

Reconfigurable quantum photonic circuits based on quantum dots

ADAM MCCAW,¹ JACOB EWANIUK¹, BHAVIN J. SHASTRI,^{1,2} AND NIR ROTENBERG^{1,*}

¹Centre for Nanophotonics, Department of Physics, Engineering Physics, & Astronomy, Queen's University, 64 Bader Lane, Kingston, Ontario, Canada K7L 3N6

²Vector Institute, Toronto, Ontario, Canada M5G 1M1

*nir.rotenberg@queensu.ca

Abstract: Quantum photonic integrated circuits, composed of linear-optical elements, offer an efficient way for encoding and processing quantum information on-chip. At their core, these circuits rely on reconfigurable phase shifters, typically constructed from classical components such as thermo- or electro-optical materials, while quantum solid-state emitters such as quantum dots are limited to acting as single-photon sources. Here, we demonstrate the potential of quantum dots as reconfigurable phase shifters. We use numerical models based on established literature parameters to show that circuits utilizing these emitters enable high-fidelity operation and are scalable. Despite the inherent imperfections associated with quantum dots, such as imperfect coupling, dephasing, or spectral diffusion, our optimization shows that these do not significantly impact the unitary infidelity. Specifically, they do not increase the infidelity by more than 0.001 in circuits with up to 10 modes, compared to those affected only by standard nanophotonic losses and routing errors. For example, we achieve fidelities of 0.9998 in quantum-dot-based circuits enacting controlled-phase and -not gates without any redundancies. These findings demonstrate the feasibility of quantum emitter-driven quantum information processing and pave the way for cryogenically-compatible, fast, and low-loss reconfigurable quantum photonic circuits.

1. Introduction

Reconfigurable quantum photonic integrated circuits (qPICs) are versatile tools capable of simulating molecular dynamics [1], executing quantum logic [2], and generating multidimensional entanglement [3–7]. They utilize quantum properties such as entanglement and indistinguishability for information processing, which is unachievable through classical means. This capability is crucial for developing emerging quantum communication and computation technologies.

To date, qPICs have predominantly operated at room temperature, harnessing the advancements of foundry photonics to create increasingly complex devices [8, 9]. As depicted in Fig. 1, the core of these circuits is a mesh of Mach-Zehnder interferometers (MZIs) [10], where each MZI is comprised of two directional couplers and two phase shifters (see Fig. 1b), typically thermo-optical in nature [11, 12]. That is, this mesh is fully classical, based on low-loss and highly accurate (albeit slow and hot) phase shifters. Though it is susceptible to unbalanced nanophotonic imperfections, such as some losses and imperfect routing, high-fidelity operation is achievable with redundancy and optimization [13–18].

The quantum nature of qPICs stems from the individual photons that propagate through the circuits. Single photons are often generated by optical nonlinearities such as spontaneous parametric down-conversion, which is compatible with room-temperature chips but inherently probabilistic [19–21]. In contrast, single-photon sources based on solid-state quantum emitters, such as the quantum dots (QDs) we consider, can operate on-demand but require cryogenic temperatures [22–25]. Similarly, high-efficiency integrated single-photon detectors also necessitate a cryogenic environment [26–28]. As a result, both state-of-the-art sources and detectors cannot be heterogeneously integrated with qPICs and instead currently rely on lossy interconnects [29].

Here, we propose that QDs can be used not only as single-photon sources, but also as

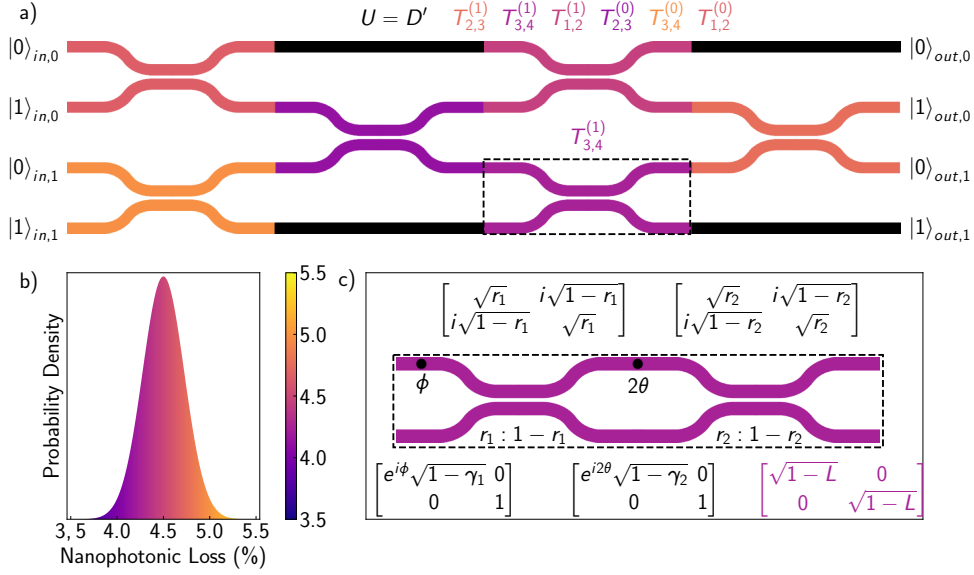


Fig. 1. Scalable Reconfigurable MZI Meshes. (a) 4-mode MZI mesh colored to represent nanophotonic losses in each interferometer. (b) Normal distribution for nanophotonic loss with a mean of 4.5% and standard deviation that is 5% of the mean. (c) A zoom-in on the basic component of the mesh (dashed region in a), a MZI with two phase shifters ϕ and 2θ and two imperfect beam splitters along with the imperfect transfer matrices for each component and for the overall nanophotonic loss.

reconfigurable phase shifters for creating fast, cryogenically-compatible meshes. Our model of QD-based qPICs incorporates standard nanophotonic imperfections, such as losses and routing errors, along with QD-specific non-idealities, like imperfect interactions and both fast and slow noise processes. We use this model to evaluate the fidelity of both the resultant unitary operations and the desired output states. Our findings reveal that these QD-based meshes can be optimized to achieve remarkable scalability, with a unitary infidelity less than 0.001 for circuits up to 10×10 in dimension, using state-of-the-art QD parameters from the literature. We further consider QD-based controlled-phase and -not gates as examples, where we find that state-of-the-art circuits process logical states with fidelities of 0.9998. In sum, our results offer a roadmap to cryogenically-compatible, reconfigurable qPICs based on solid-state quantum emitters.

2. Quantum-emitter phase shifters

The scattering of photons from a quantum emitter embedded in a nanophotonic waveguide is a complex process [30] that may modulate the photons' amplitude or phase [31, 32] or, when more than a single photon is present, induce complex correlations [33, 34]. The exact response depends on the properties of the emitter and the efficiency with which it couples to the various available modes, as sketched in Fig. 2a, yet in the most general case, an input single-photon state with phase φ_0 , $|1\rangle_{\text{in}} = |\varphi_0\rangle$, will scatter into the mixed state,

$$|1\rangle_{\text{out}} = \begin{cases} \alpha_{\text{co}} |\varphi_0 + \Delta\varphi\rangle \\ \alpha_{\text{inc}} |\varphi_0\rangle \end{cases}, \quad (1)$$

where, in the presence of losses the sum of the probabilities to scatter coherently and incoherently, $|\alpha_{\text{co}}|^2$ and $|\alpha_{\text{inc}}|^2$, do not sum to unity.

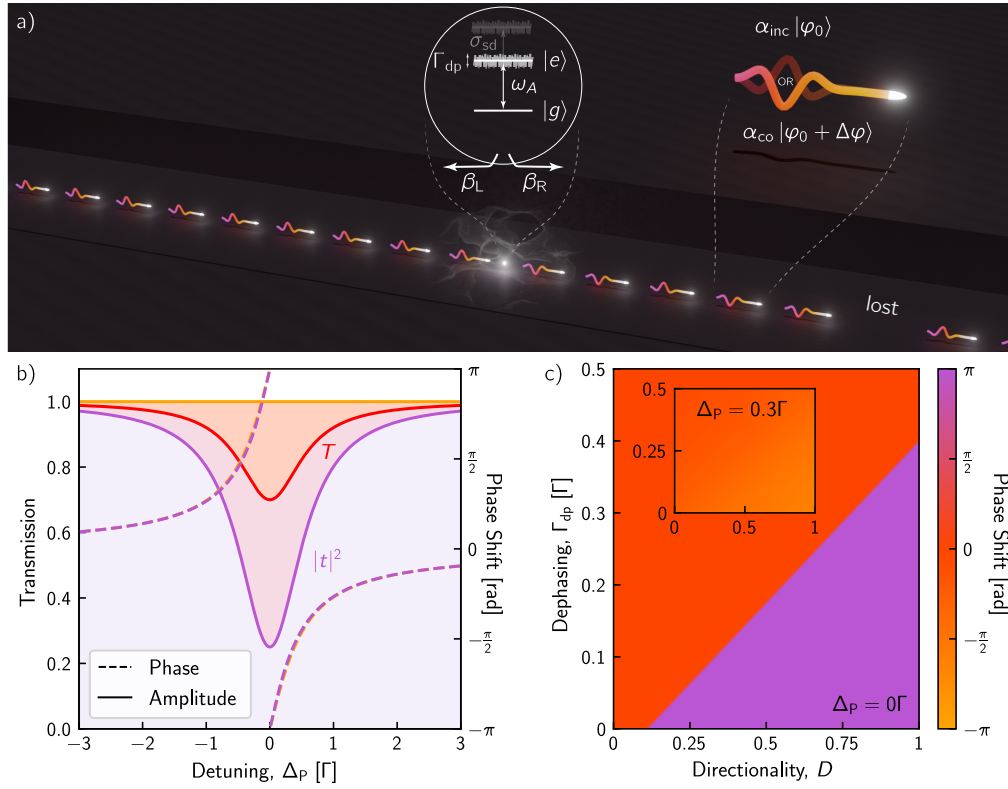


Fig. 2. Waveguide-coupled chiral quantum dots (QDs). (a) A QD chirally-coupled to a waveguide with its forward direction to the right, $\beta_R \gg \beta_L$, imparts a phase shift $\Delta\varphi$ on coherently-scattered photons but not to those with which it interacts incoherently (due to fast dephasing). If $\beta_R < 1$, then some photons are either reflected or scattered out of the waveguide. (b) Transmission spectrum of the interaction shown in (a). In the ideal case ($\beta_R = 1$ and no noise, solid orange curve) all photons are transmitted, while if $\beta_R = 0.9$ and $\Gamma_{dp} = 0.1\Gamma$ then the presence of the QD will be imprinted on the total transmission spectrum (solid red curve) and the coherent transmission spectrum (solid purple curve). The associated phase shift applied to the coherently-scattered photons in both the ideal (orange) and non-ideal (purple) scenarios is shown in dashed curve (right axis), which are nearly identical. (c) On-resonance phase shift as a function of directionality and dephasing rate (inset: similar map for a photon-emitter detuning of $\Delta_p = 0.3\Gamma$). The large region over which $\Delta\varphi = \pi$ demonstrates the robustness of QD-based phase shifters.

The description of Eq. 1 only holds if the single-photon pulse is not reshaped during scattering, requiring that the pulse linewidth σ_p be much shorter than that of the emitter. More formally, we require that $\sigma_p \leq \Gamma/1000$, ensuring the phase shifter response is linear (see SI for more information).

In this regime, the single-photon transmission coefficient t and total transmission T are the

same as that of a weak coherent beam (see SI for derivation),

$$t = 1 - \Gamma\beta_R \frac{\Gamma_2 + i\Delta_p}{\Gamma_2^2 + \Delta_p^2}, \quad (2)$$

$$T = 1 - 2\Gamma\Gamma_2 \frac{\beta_R(1 - \beta_R)}{(\Gamma_2^2 + \Delta_p^2)}, \quad (3)$$

where β_R is the coupling efficiency for right-traveling photons (with a total coupling efficiency $\beta = \beta_R + \beta_L$), Δ_p is the detuning between the photon and emitter-transition frequencies, Γ is the decay rate of the emitter, and $\Gamma_2 = \Gamma/2 + \Gamma_{dp}$ where Γ_{dp} is the pure dephasing rate (i.e. fast noise). We note that in the presence of dephasing, $T \neq |t|^2$ (c.f. Fig. 2b), and that the emitter might also suffer from slow noise leading to spectral diffusion with a characteristic linewidth σ_{sd} .

Eqs. 2 and 3 allow us to quantify the results of the scattering. The coefficients, α_{co} and α_{inc} , are related to the transmission, as shown in Fig. 2b. In the ideal case, where $\beta_R = 1$ and $\Gamma_{dp} = 0$, the transmission is always unity (orange curve) meaning that $\alpha_{co} = 1$ and $\alpha_{inc} = 0$. Conversely, in the presence of losses and/or dephasing, the situation is more complex with $\alpha_{co} = |t|^2$ and $\alpha_{inc} = T - |t|^2$ as shown by the purple and red curves.

The phase of the coherently-scattered photons is likewise calculated from $\Delta\varphi = \arg(t)$, here shown in dashed curves in Fig. 2b corresponding to the ideal and non-ideal scenarios. As can be seen, the imparted phase shift is nearly identical in both cases, spanning the full 2π and demonstrating the robustness of emitter-based phase shifters. Full, 2D maps of the induced phase shift on resonance, $\Delta_p = 0$, and at $\Delta_p = 0.3\Gamma$, are shown in Figs. 2c and d, respectively, again demonstrating that a 2π phase change is possible even when the directionality is below $D < 0.25$ or the dephasing rate is above $\Gamma_{dp} > 0.3\Gamma$. However, this range also depends on emitter parameters such as β . Corresponding maps of $|\alpha_{co}|^2$ are presented in the SI. Together, these enable us to pick an emitter detuning for each desired phase shift, and then calculate the scattered state (c.f. Eq. 1).

3. QD-based qPICs

Having seen that quantum emitters such as QDs can serve as reconfigurable phase shifters, we quantify the performance of qPICs based on this technology. To do so, we first compare how well we can reproduce any unitary (i.e. operation) with our emitter-based qPICs relative to the ideal, summarizing the results in Fig. 3. Here, we show the dependence of the mean circuit infidelity \mathcal{I} (i.e. error) as a function of (a) β , (b) D , (c) Γ_{dp} and (d) σ_{sd} , where, in all, \mathcal{I} is limited by the nanophotonic errors as noted in the caption.

As an example, consider the β -dependence of \mathcal{I} , shown in Fig. 3a. In dashed curves, we show the infidelity of the non-ideal unitary U_{non} , constructed following the procedure of [10] using the set of phases $\{2\theta_i, \phi_i\}$ (c.f. Fig. 1c) calculated for the ideal circuit, but with imperfections subsequently added (see SI for details). This corresponds to the offline training of a photonic circuit. For each coupling efficiency β , we compare 100 non-ideal unitaries U_{non} to the ideal U to calculate [10]

$$\mathcal{I} = 1 - \left| \frac{\text{tr}(U^\dagger U_{non})}{\sqrt{N \text{tr}(U_{non}^\dagger U_{non})}} \right|^2, \quad (4)$$

which we then average. In the figure, we show the cases for $N = 2, 6, 10$ mode circuits, where in all cases, we observe a monotonic increase from a baseline \mathcal{I} due to the nanophotonic imperfections when $\beta = 1$, to near-unity error when the coupling efficiency is $\beta = 0.5$.

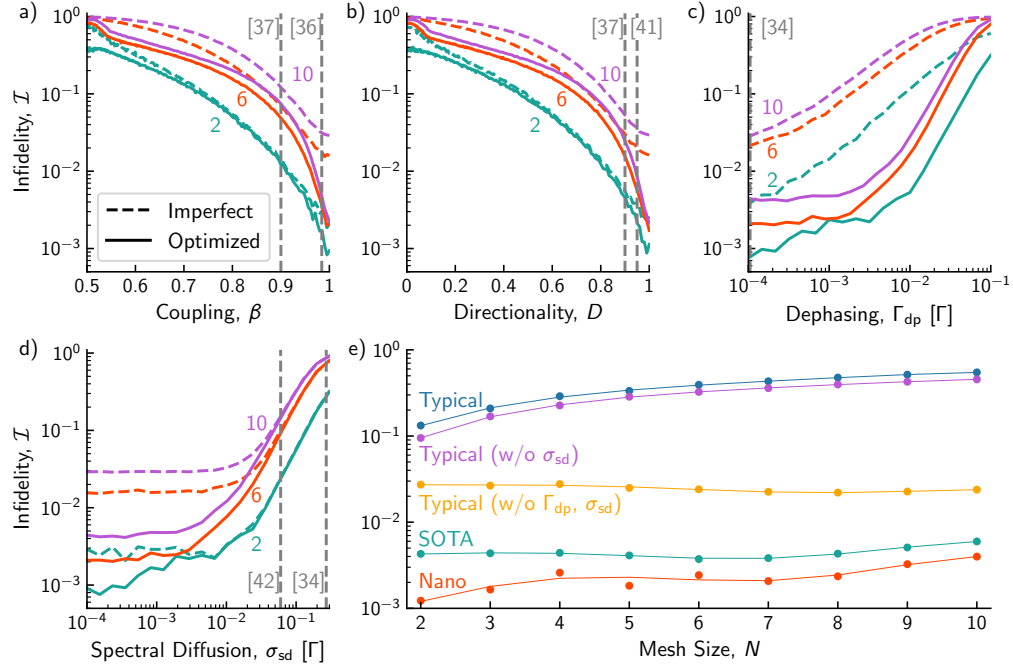


Fig. 3. The effects of QD imperfections on circuit unitary infidelity. All plots have 4.5% nanophotonic loss and 4% beam splitter error. (a-d) With no other QD imperfections, we examine the effects of (a) coupling efficiency, β , (b) directionality, D , (c) pure dephasing rate, Γ_{dp} , and (d) spectral diffusion, σ_{sd} on infidelity, showing both the imperfect (dashed) and optimized (solid) results. In all cases, state-of-the-art QD parameters from literature are indicated by vertical dashed lines. (e) The infidelity of QD-based qPICs as a function of mesh size ranging from $N = 2$ to 10 for circuits suffering only from nanophotonic imperfections (red), as well as those that additionally suffer from state-of-the-art QD imperfections (green) or typical QD imperfections (blue). See Table 1 for QD parameter values. Also shown are infidelities for circuits based on typical QDs but no noise (orange) or with only fast dephasing (purple), demonstrating that circuit errors are largely due to dephasing.

Encouragingly, we can optimize the performance of the emitter-based qPICs, following a fast and efficient routine that finds the optimal set $\{2\theta_i, \phi_i\}$ at once [35]. This procedure results in an optimized unitary U_{opt} that, together with Eq. 4, enables us to again calculate \mathcal{I} , which we show as solid curves in Fig. 3. In all cases, we observe a significant reduction in errors due to the optimization, with this reduction particularly pronounced for larger circuit sizes and in near-optimal conditions. For example, in Fig. 3a (and b-d), as $\beta \rightarrow 1$ corresponding to state-of-the-art performance (dashed line) [36], we observe almost no increased infidelity as the circuit size increases. A similar dependence is observed as D and Γ_{dp} are scanned (Fig. 3b and c, respectively), while spectral diffusion only begins affecting the performance when $\sigma_{sd} \gtrsim 0.01\Gamma$ (Fig. 3d).

Overall, we summarize the circuit scaling in Fig. 3e, where we plot the raw and optimized infidelity as a function of circuit size, both using typical and state-of-the-art parameters (see Table 1). For typical values (blue curve), we see that the infidelity quickly approaches unity, yet by adding imperfections sequentially (purple and orange curves), we see that this is almost entirely caused by the residual dephasing. This is consistent with the optimized state-of-the-art qPIC performance (green curve), where $\mathcal{I} < 0.006$ is observed for all circuits simulated (up to

$N = 10$), as several recent experiments based on QDs have measured $\Gamma_{\text{dp}} \approx 0$ [34, 37–40].

Table 1. State-of-the-art and typical quantum dot parameters. Listed parameters include coupling, β , directionality, D , dephasing, Γ_{dp} , spectral diffusion detuning standard deviation, σ_{sd} . For more details on these parameters, see SI.

	Typical	Ref(s)	State-of-the-art	Ref(s)
β	0.90	[37]	0.98	[36]
D	0.90	[37]	0.95	[41]
Γ_{dp}	0.01Γ	[34]	0Γ	[34, 37–40]
σ_{sd}	0.06Γ	[42]	0Γ	[43, 44]

4. Examples: CZ gate

To demonstrate the possibilities of emitter-based qPICs, we consider the controlled-phase (CZ) gate, which can be used to generate entanglement [45], and, in the SI, a similar realization of a controlled-not (CNOT) gate that enables universal quantum computation [46]. A linear-optical unheralded CZ gate can be realized on a 6×6 mesh [45], and in Fig. 4a we plot the unitary infidelity \mathcal{I} (Eq. 4) calculated as a function of Γ_{dp} for circuits with only nanophotonic imperfections (red curve, no dephasing), the addition of typical QD imperfections (blue curve), and state-of-the-art QD imperfections (green curve), where for the latter two cases the dephasing varies along the horizontal axis (different from Tab. 1). For typical parameters, $\mathcal{I} > 0.25$ regardless of the dephasing rate, consistent with Fig. 3. Interestingly, the optimized circuit based on typical QD parameters is nearly identical to that based on state-of-the-art when $\Gamma_{\text{dp}} > 0.01\Gamma$, meaning that in this regime, the effect of dephasing dominates all other emitter parameters. In contrast, the optimized curve for state-of-the-art parameters, including all QD imperfections (green), tends toward that for conventional phase shifters (red) in the limit that dephasing approaches its state-of-the-art value ($\Gamma_{\text{dp}} \approx 0$). Additionally, while circuits with only nanophotonic imperfections achieve an optimized unitary infidelity of 0.0023, independent of Γ_{dp} , it increases only to 0.0037 at $\Gamma_{\text{dp}} = 10^{-8}\Gamma$, 0.0065 at $\Gamma_{\text{dp}} = 10^{-6}\Gamma$, and remains less than 0.01 up to $\Gamma_{\text{dp}} \sim 10^{-5}\Gamma$.

More significantly, we consider the fidelity with which logical states are processed by the CZ gate (\mathcal{F}) across Figs. 4b-d. Specifically, here we present the post-selected 4×4 matrices for the CZ gate in the computational basis for nanophotonic, state-of-the-art, and typical imperfections (as in Tab. 1). The state fidelity is the chance the CZ gate produces the correct output in the computational basis for any given input, given that the output is in the computational basis. It is shown below the corresponding matrix in each case (state fidelity calculation details are provided in the SI). Although the performance of the typical circuit (Fig. 4d) significantly differs from the nanophotonic-only (Fig. 4b), as expected, the circuit based on state-of-the-art QD parameters (Fig. 4c) achieves $\mathcal{F} = 0.9998$, matching the performance of circuits constructed from traditional phase shifters. A similar figure and result is presented in the SI for a CNOT gate. As demonstrated by these results, the state fidelity is typically better than the unitary infidelity, reinforcing the viability of QD-based qPICs.

5. Conclusions

Our research demonstrates that qPICs built with reconfigurable QD-phase shifters can perform comparable to those using classical phase shifters. Notably, we show that with state-of-the-art QD parameters, circuits can be scaled up to 10 modes without significant increases in unitary infidelity. This advancement allows QD-based qPICs to efficiently perform operations such as

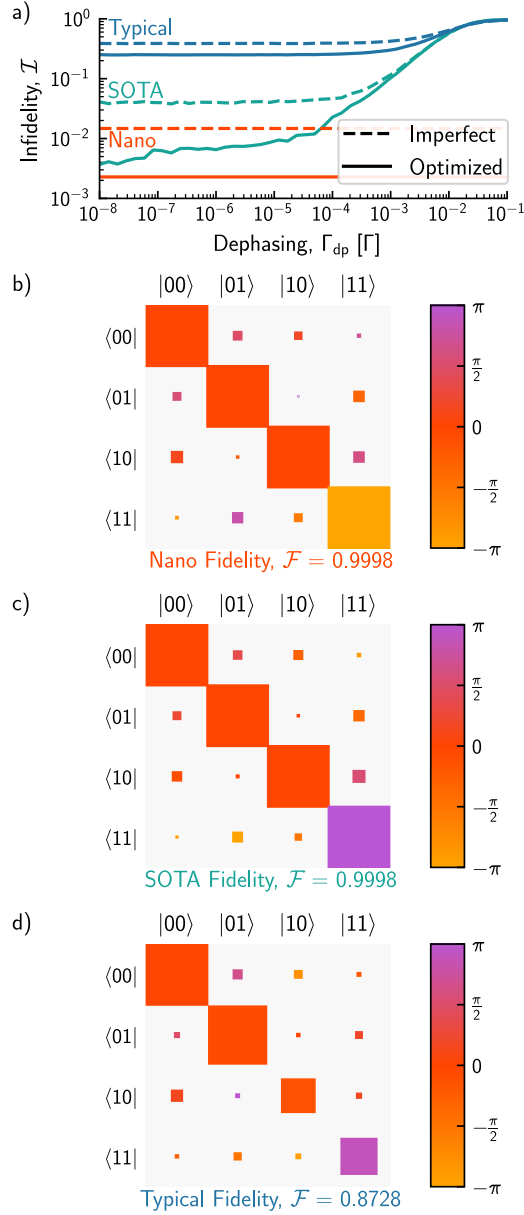


Fig. 4. Unheralded CZ gate performance for nanophotonic, state-of-the-art, and typical imperfections (as previously explained in Fig. 3 and Tab. 1). (a) Imperfect (dashed) and optimized (solid) unitary infidelities (\mathcal{I} , c.f. Eq. 4) as a function of dephasing. All QD parameters other than Γ_{dp} are as listed in Tab. 1. Since circuits with only nanophotonic imperfections do not suffer from dephasing, their performance is flat in Γ_{dp} . (b-d) Optimized nanophotonic, state-of-the-art, and typical post-selected 4×4 computational basis matrices for the unheralded CZ gate, with corresponding conditional output state fidelities listed below each matrix.

multi-qubit gates, as demonstrated in our study, and to simulate molecular dynamics [47]. The performance of these circuits could be further enhanced by incorporating redundancies, where

extra MZIs and phase shifters provide better compensation for imperfections [13, 15–17].

However, the practicality of fabricating and managing circuits with numerous emitters remains a topic of inquiry. We recognize that while QDs are the only quantum emitters currently integrated into photonic circuits, alternative technologies based on single organic molecules [48, 49] and defects in diamond [50, 51], silicon [52], or silicon carbide [53, 54] are rapidly maturing. Recent experiments with QDs have successfully demonstrated the integration of deterministic QD-based single-photon sources with qPICs [55, 56], and independent control of multiple emitters within a circuit [57, 58], respectively. These advancements, alongside the ability to pre-select specific QDs and integrate them deterministically within a circuit [59–64], open the door to larger-scale implementations where emitters would function both as sources and processing elements. Such circuits would be entirely cryogenic, and thus compatible with deterministic sources and detectors, with phase shifters whose operational speeds are determined by emitter lifetimes, potentially enabling GHz rate operation with mild enhancement [34, 43].

Funding. Content in the funding section will be generated entirely from details submitted to Prism. Authors may add placeholder text in the manuscript to assess length, but any text added to this section in the manuscript will be replaced during production and will display official funder names along with any grant numbers provided. If additional details about a funder are required, they may be added to the Acknowledgments, even if this duplicates information in the funding section. See the example below in Acknowledgements. For preprint submissions, please include funder names and grant numbers in the manuscript.

Acknowledgments. The authors thank J. Carolan for generating stimulating discussions on quantum photonic integrated circuits, and gratefully acknowledge support by the Natural Sciences and Engineering Research Council of Canada (NSERC), the Canadian Foundation for Innovation (CFI), the Vector Institute, and Queen's University.

Disclosures. The authors declare no conflicts of interest.

Data availability. Data availability statements are not required for preprint submissions.

Supplemental document. See Supplement 1 for supporting content.

References

1. C. Sparrow, E. Martín-López, N. Maraviglia, A. Neville, C. Harrold, J. Carolan, Y. N. Joglekar, T. Hashimoto, N. Matsuda, J. L. O'Brien *et al.*, “Simulating the vibrational quantum dynamics of molecules using photonics,” *Nature* **557**, 660–667 (2018).
2. J. Carolan, C. Harrold, C. Sparrow, E. Martín-López, N. J. Russell, J. W. Silverstone, P. J. Shadbolt, N. Matsuda, M. Oguma, M. Itoh *et al.*, “Universal linear optics,” *Science* **349**, 711–716 (2015).
3. J. Wang, S. Paesani, Y. Ding, R. Santagati, P. Skrzypczyk, A. Salavrakos, J. Tura, R. Augusiak, L. Mančinska, D. Bacco *et al.*, “Multidimensional quantum entanglement with large-scale integrated optics,” *Science* **360**, 285–291 (2018).
4. J. C. Adcock, C. Vigliar, R. Santagati, J. W. Silverstone, and M. G. Thompson, “Programmable four-photon graph states on a silicon chip,” *Nat. Commun.* **10**, 3528 (2019).
5. D. Llewellyn, Y. Ding, I. I. Faruque, S. Paesani, D. Bacco, R. Santagati, Y.-J. Qian, Y. Li, Y.-F. Xiao, M. Huber *et al.*, “Chip-to-chip quantum teleportation and multi-photon entanglement in silicon,” *Nat. Phys.* **16**, 148–153 (2020).
6. C. Vigliar, S. Paesani, Y. Ding, J. C. Adcock, J. Wang, S. Morley-Short, D. Bacco, L. K. Oxenløwe, M. G. Thompson, J. G. Rarity *et al.*, “Error-protected qubits in a silicon photonic chip,” *Nat. Phys.* **17**, 1137–1143 (2021).
7. J. Bao, Z. Fu, T. Pramanik, J. Mao, Y. Chi, Y. Cao, C. Zhai, Y. Mao, T. Dai, X. Chen *et al.*, “Very-large-scale integrated quantum graph photonics,” *Nat. Photonics* **17**, 573–581 (2023).
8. W. Bogaerts, D. Pérez, J. Capmany, D. A. Miller, J. Poon, D. Englund, F. Morichetti, and A. Melloni, “Programmable photonic circuits,” *Nature* **586**, 207–216 (2020).
9. H. Hou, P. Xu, Z. Zhou, and H. Su, “Hardware Error Correction for MZI-Based Matrix Computation,” *Micromachines* **14**, 955 (2023).
10. W. R. Clements, P. C. Humphreys, B. J. Metcalf, W. S. Kolthammer, and I. A. Walmsley, “Optimal design for universal multiport interferometers,” *Optica* **3**, 1460–1465 (2016).
11. J. Parra, J. Hurtado, A. Griol, and P. Sanchis, “Ultra-low loss hybrid ITO/Si thermo-optic phase shifter with optimized power consumption,” *Opt. Express* **28**, 9393–9404 (2020).
12. M. Jacques, A. Samani, E. El-Fiky, D. Patel, Z. Xing, and D. V. Plant, “Optimization of thermo-optic phase-shifter design and mitigation of thermal crosstalk on the SOI platform,” *Opt. Express* **27**, 10456–10471 (2019).

13. D. A. B. Miller, "Perfect optics with imperfect components," *Optica* **2**, 747–750 (2015).
14. J. Mower, N. C. Harris, G. R. Steinbrecher, Y. Lahini, and D. Englund, "High-fidelity quantum state evolution in imperfect photonic integrated circuits," *Phys. Rev. A* **92**, 032322 (2015).
15. C. M. Wilkes, X. Qiang, J. Wang, R. Santagati, S. Paesani, X. Zhou, D. A. B. Miller, G. D. Marshall, M. G. Thompson, and J. L. O'Brien, "60 dB high-extinction auto-configured Mach–Zehnder interferometer," *Opt. Lett.* **41**, 5318–5321 (2016).
16. S. Pai, B. Bartlett, O. Solgaard, and D. A. B. Miller, "Matrix Optimization on Universal Unitary Photonic Devices," *Phys. Rev. Appl.* **11**, 064044 (2019).
17. S. Bandyopadhyay, R. Hamerly, and D. Englund, "Hardware error correction for programmable photonics," *Optica* **8**, 1247–1255 (2021).
18. F. Shokraneh, M. Sanadgol Nezami, and O. Liboiron-Ladouceur, "Theoretical and Experimental Analysis of a 44 Reconfigurable MZI-Based Linear Optical Processor," *J. Light. Technol.* pp. 1–1 (2021).
19. C. Wagenknecht, C.-M. Li, A. Reingruber, X.-H. Bao, A. Goebel, Y.-A. Chen, Q. Zhang, K. Chen, and J.-W. Pan, "Experimental demonstration of a heralded entanglement source," *Nat. Photonics* **4**, 549–552 (2010).
20. F. Kaneda, K. Garay-Palmett, A. B. U'Ren, and P. G. Kwiat, "Heralded single-photon source utilizing highly nondegenerate, spectrally factorable spontaneous parametric downconversion," *Opt. Express* **24**, 10733–10747 (2016).
21. C. Couteau, "Spontaneous parametric down-conversion," *Contemp. Phys.* **59**, 291–304 (2018).
22. N. Somaschi, V. Giesz, L. De Santis, J. Loredò, M. P. Almeida, G. Hornecker, S. L. Portalupi, T. Grange, C. Anton, J. Demory *et al.*, "Near-optimal single-photon sources in the solid state," *Nat. Photonics* **10**, 340–345 (2016).
23. P. Senellart, G. Solomon, and A. White, "High-performance semiconductor quantum-dot single-photon sources," *Nat. Nanotechnol.* **12**, 1026–1039 (2017).
24. R. S. Daveau, K. C. Balram, T. Pregolato, J. Liu, E. H. Lee, J. D. Song, V. Verma, R. Mirin, S. W. Nam, L. Midolo *et al.*, "Efficient fiber-coupled single-photon source based on quantum dots in a photonic-crystal waveguide," *Optica* **4**, 178–184 (2017).
25. R. Uppu, F. T. Pedersen, Y. Wang, C. T. Olesen, C. Papon, X. Zhou, L. Midolo, S. Scholz, A. D. Wieck, A. Ludwig *et al.*, "Scalable integrated single-photon source," *Sci. Adv.* **6**, eabc8268 (2020).
26. W. H. Pernice, C. Schuck, O. Minaeva, M. Li, G. Goltsman, A. Sergienko, and H. Tang, "High-speed and high-efficiency travelling wave single-photon detectors embedded in nanophotonic circuits," *Nat. Commun.* **3**, 1325 (2012).
27. D. Rosenberg, A. Kerman, R. Molnar, and E. Dauler, "High-speed and high-efficiency superconducting nanowire single photon detector array," *Opt. Express* **21**, 1440–1447 (2013).
28. I. Esmail Zadeh, J. W. Los, R. Gourgues, V. Steinmetz, G. Bulgarini, S. M. Dobrovolskiy, V. Zwiller, and S. N. Dorenbos, "Single-photon detectors combining high efficiency, high detection rates, and ultra-high timing resolution," *APL Photonics* **2** (2017).
29. Y. Wang, C. F. D. Faurby, F. Ruf, P. I. Sund, K. Nielsen, N. Volet, M. J. R. Heck, N. Bart, A. D. Wieck, A. Ludwig, L. Midolo, S. Paesani, and P. Lodahl, "Deterministic photon source interfaced with a programmable silicon-nitride integrated circuit," *npj Quantum Inf.* **9** (2023).
30. A. S. Sheremet, M. I. Petrov, I. V. Iorsh, A. V. Poshakinskiy, and A. N. Poddubny, "Waveguide quantum electrodynamics: Collective radiance and photon-photon correlations," *Rev. Mod. Phys.* **95**, 015002 (2023).
31. H. Le Jeannic, T. Ramos, S. F. Simonsen, T. Pregolato, Z. Liu, R. Schott, A. D. Wieck, A. Ludwig, N. Rotenberg, J. J. García-Ripoll *et al.*, "Experimental reconstruction of the few-photon nonlinear scattering matrix from a single quantum dot in a nanophotonic waveguide," *Phys. Rev. Lett.* **126**, 023603 (2021).
32. M. J. Staunstrup, A. Tiranov, Y. Wang, S. Scholz, A. D. Wieck, A. Ludwig, L. Midolo, N. Rotenberg, P. Lodahl, and H. L. Jeannic, "Direct observation of non-linear optical phase shift induced by a single quantum emitter in a waveguide," *arXiv preprint arXiv:2305.06839* (2023).
33. J.-T. Shen and S. Fan, "Strongly Correlated Two-Photon Transport in a One-Dimensional Waveguide Coupled to a Two-Level System," *Phys. Rev. Lett.* **98**, 153003 (2007).
34. H. Le Jeannic, A. Tiranov, J. Carolan, T. Ramos, Y. Wang, M. H. Appel, S. Scholz, A. D. Wieck, A. Ludwig, N. Rotenberg *et al.*, "Dynamical photon–photon interaction mediated by a quantum emitter," *Nat. Phys.* **18**, 1191–1195 (2022).
35. M. J. Powell *et al.*, "The BOBYQA algorithm for bound constrained optimization without derivatives," *Camb. NA Rep. NA2009/06*, Univ. Cambridge, Camb. **26** (2009).
36. M. Arcari, I. Söllner, A. Javadi, S. Lindskov Hansen, S. Mahmoodian, J. Liu, H. Thyrestrup, E. H. Lee, J. D. Song, S. Stobbe, and P. Lodahl, "Near-unity coupling efficiency of a quantum emitter to a photonic crystal waveguide," *Phys. Rev. Lett.* **113**, 093603 (2014).
37. I. Söllner, S. Mahmoodian, S. L. Hansen, L. Midolo, A. Javadi, G. Kiršanskė, T. Pregolato, H. El-Ella, E. H. Lee, J. D. Song, S. Stobbe, and P. Lodahl, "Deterministic photon–emitter coupling in chiral photonic circuits," *Nat. Nanotechnol.* **10**, 775–778 (2015).
38. W. Langbein, P. Borri, U. Woggon, V. Stavarache, D. Reuter, and A. Wieck, "Radiatively limited dephasing in inas quantum dots," *Phys. Rev. B* **70**, 033301 (2004).
39. C. Matthiesen, A. N. Vamivakas, and M. Atatüre, "Subnatural linewidth single photons from a quantum dot," *Phys. Rev. Lett.* **108**, 093602 (2012).

40. H.-S. Nguyen, G. Sallen, C. Voisin, P. Roussignol, C. Diederichs, and G. Cassabois, "Ultra-coherent single photon source," *Appl. Phys. Lett.* **99** (2011).
41. R. J. Coles, D. M. Price, J. E. Dixon, B. Royall, E. Clarke, P. Kok, M. S. Skolnick, A. M. Fox, and M. N. Makhonin, "Chirality of nanophotonic waveguide with embedded quantum emitter for unidirectional spin transfer," *Nat. Commun.* **7**, 11183 (2016).
42. H. Thyrrstrup, G. Kiršanskė, H. Le Jeannic, T. Pregolato, L. Zhai, L. Raahauge, L. Midolo, N. Rotenberg, A. Javadi, R. Schott, A. D. Wieck, A. Ludwig, M. C. Löbl, I. Söllner, R. J. Warburton, and P. Lodahl, "Quantum Optics with Near-Lifetime-Limited Quantum-Dot Transitions in a Nanophotonic Waveguide," *Nano Lett.* **18**, 1801–1806 (2018).
43. F. T. Pedersen, Y. Wang, C. T. Olesen, S. Scholz, A. D. Wieck, A. Ludwig, M. C. Löbl, R. J. Warburton, L. Midolo, R. Uppu *et al.*, "Near transform-limited quantum dot linewidths in a broadband photonic crystal waveguide," *ACS Photonics* **7**, 2343–2349 (2020).
44. A. V. Kuhlmann, J. Houel, A. Ludwig, L. Greuter, D. Reuter, A. D. Wieck, M. Poggio, and R. J. Warburton, "Charge noise and spin noise in a semiconductor quantum device," *Nat. Phys.* **9**, 570–575 (2013).
45. N. Kiesel, C. Schmid, U. Weber, R. Ursin, and H. Weinfurter, "Linear Optics Controlled-Phase Gate Made Simple," *Phys. Rev. Lett.* **95**, 210505 (2005).
46. J. L. O'Brien, "Optical Quantum Computing," *Science* **318**, 1567–1570 (2007).
47. P. J. Ollitrault, A. Miessen, and I. Tavernelli, "Molecular quantum dynamics: A quantum computing perspective," *Accounts Chem. Res.* **54**, 4229–4238 (2021).
48. P. Türschmann, N. Rotenberg, J. Renger, I. Harder, O. Lohse, T. Utikal, S. Götzinger, and V. Sandoghdar, "Chip-based all-optical control of single molecules coherently coupled to a nanoguide," *Nano Lett.* **17**, 4941–4945 (2017).
49. C. Toninelli, I. Gerhardt, A. Clark, A. Reserbat-Plantey, S. Götzinger, Z. Ristanović, M. Colautti, P. Lombardi, K. Major, I. Deperasińska *et al.*, "Single organic molecules for photonic quantum technologies," *Nat. Mater.* **20**, 1615–1628 (2021).
50. R. E. Evans, M. K. Bhaskar, D. D. Sukachev, C. T. Nguyen, A. Sipahigil, M. J. Burek, B. Machielse, G. H. Zhang, A. S. Zibrov, E. Bielejec *et al.*, "Photon-mediated interactions between quantum emitters in a diamond nanocavity," *Science* **362**, 662–665 (2018).
51. P. K. Shandilya, S. Flågan, N. C. Carvalho, E. Zohari, V. K. Kavatamane, J. E. Losby, and P. E. Barclay, "Diamond integrated quantum nanophotonics: spins, photons and phonons," *J. Light. Technol.* **40**, 7538–7571 (2022).
52. M. Veldhorst, C. Yang, J. Hwang, W. Huang, J. Dehollain, J. Muhonen, S. Simmons, A. Laucht, F. Hudson, K. M. Itoh *et al.*, "A two-qubit logic gate in silicon," *Nature* **526**, 410–414 (2015).
53. D. M. Lukin, C. Dory, M. A. Guidry, K. Y. Yang, S. D. Mishra, R. Trivedi, M. Radulaski, S. Sun, D. Vercruysee, G. H. Ahn *et al.*, "4H-silicon-carbide-on-insulator for integrated quantum and nonlinear photonics," *Nat. Photonics* **14**, 330–334 (2020).
54. D. M. Lukin, M. A. Guidry, and J. Vučković, "Integrated Quantum Photonics with Silicon Carbide: Challenges and Prospects," *PRX Quantum* **1**, 020102 (2020).
55. A. Chanana, H. Larocque, R. Moreira, J. Carolan, B. Guha, E. G. Melo, V. Anant, J. Song, D. Englund, D. J. Blumenthal, K. Srinivasan, and M. Davanco, "Ultra-low loss quantum photonic circuits integrated with single quantum emitters," *Nat. Commun.* **13**, 7693 (2022).
56. J.-H. Kim, S. Aghaeimeibodi, C. J. K. Richardson, R. P. Leavitt, D. Englund, and E. Waks, "Hybrid integration of solid-state quantum emitters on a silicon photonic chip," *Nano Lett.* **17**, 7394–7400 (2017).
57. C. Papon, Y. Wang, R. Uppu, S. Scholz, A. D. Wieck, A. Ludwig, P. Lodahl, and L. Midolo, "Independent operation of two waveguide-integrated quantum emitters," *Phys. Rev. Appl.* **19**, L061003 (2023).
58. X.-L. Chu, C. Papon, N. Bart, A. D. Wieck, A. Ludwig, L. Midolo, N. Rotenberg, and P. Lodahl, "Independent electrical control of two quantum dots coupled through a photonic-crystal waveguide," *Phys. Rev. Lett.* **131**, 033606 (2023).
59. T. Pregolato, X.-L. Chu, T. Schröder, R. Schott, A. D. Wieck, A. Ludwig, P. Lodahl, and N. Rotenberg, "Deterministic positioning of nanophotonic waveguides around single self-assembled quantum dots," *APL Photonics* **5**, 086101 (2020).
60. S. M. Thon, M. T. Rakher, H. Kim, J. Gudat, W. T. M. Irvine, P. M. Petroff, and D. Bouwmeester, "Strong coupling through optical positioning of a quantum dot in a photonic crystal cavity," *Appl. Phys. Lett.* **94**, 111115 (2009).
61. P. Schnauber, J. Schall, S. Bounouar, T. Höhne, S.-I. Park, G.-H. Ryu, T. Heindel, S. Burger, J.-D. Song, S. Rodt, and S. Reitzenstein, "Deterministic integration of quantum dots into on-chip multimode interference beamsplitters using in situ electron beam lithography," *Nano Lett.* **18**, 2336–2342 (2018).
62. Y.-M. He, J. Liu, S. Maier, M. Emmerling, S. Gerhardt, M. Davanço, K. Srinivasan, C. Schneider, and S. Höfling, "Deterministic implementation of a bright, on-demand single-photon source with near-unity indistinguishability via quantum dot imaging," *Optica* **4**, 802–808 (2017).
63. S. Liu, Y. Wei, R. Su, R. Su, B. Ma, Z. Chen, H. Ni, Z. Niu, Y. Yu, Y. Wei, X. Wang, and S. Yu, "A deterministic quantum dot micropillar single photon source with >65% extraction efficiency based on fluorescence imaging method," *Sci. Reports* **7**, 13986 (2017).
64. J. Liu, M. I. Davanço, L. Sapienza, K. Konthasinghe, J. V. De Miranda Cardoso, J. D. Song, A. Badolato, and K. Srinivasan, "Cryogenic photoluminescence imaging system for nanoscale positioning of single quantum emitters," *Rev. Sci. Instruments* **88**, 023116 (2017).

Reconfigurable Quantum Photonic Circuits Based on Quantum Dots: supplemental document

This document provides supplementary information to “Reconfigurable Quantum Photonic Circuits Based on Quantum Dots,” including additional figures and analysis, as well as a formal mathematical description of quantum dot phase shifters.

1. TRANSMISSION AND PHASE SHIFT FROM A CHIRALLY COUPLED QUANTUM DOT

A quantum dot can be modeled as a two-level system (TLS) with a ground state $|g\rangle$ and an excited state $|e\rangle$, allowing their light-matter interaction to be modeled using the Jaynes-Cummings Hamiltonian [1] as,

$$\hat{H}_S = -\hbar\Delta_P\hat{\sigma}_{eg}\hat{\sigma}_{ge} + \hbar\omega_P\hat{f}(r)^\dagger\hat{f}(r) - \hat{d} \cdot \hat{E}(r). \quad (\text{S1})$$

The first term describes the dynamics of the emitter’s TLS where $\hat{\sigma}_{ij} = |i\rangle\langle j|$, and $\Delta_P = \omega_P - \omega_A$ is the detuning between the driving light field frequency, ω_P , and the emitter’s resonant frequency, ω_A . The second term, with the bosonic creation and annihilation operators \hat{f}^\dagger and \hat{f} , describes the energy of the free field at the position r . The final term describes the light-matter interaction between the transition dipole of the emitter, $\hat{d} = d^*\hat{\sigma}_{eg} + d\hat{\sigma}_{ge}$, and the electric field, $\hat{E} = \hat{E}^+ + \hat{E}^-$. Using the rotating wave approximation and the Lindblad master equation [2], we can determine the steady-state solution for the response of the TLS in terms of its reduced density matrix elements ρ_{ij} as,

$$\begin{aligned} \rho_{ee} &= \frac{2\Gamma_2\Omega_P^2}{\Gamma(\Gamma_2^2 + \Delta_P^2 + 4(\Gamma_2/\Gamma)\Omega_P^2)} \\ \rho_{ge} &= \frac{-\Omega_P(i\Gamma_2 + \Delta_P)}{\Gamma_2^2 + \Delta_P^2 + 4(\Gamma_2/\Gamma)\Omega_P^2} \end{aligned} \quad (\text{S2})$$

where $\Gamma = \Gamma_{ee}$ is the rate of spontaneous emission of the TLS, also corresponding to the natural linewidth of the emitter in the frequency spectra. $\Gamma_2 = \Gamma/2 + \Gamma_{dp}$ where Γ_{dp} is the rate of dephasing in the system, and $\Omega_P = d \cdot E/\hbar$ is the Rabi frequency of the light-matter system.

The electric field operators for the light field can be written in terms of the Green’s tensor $\overleftrightarrow{G}(r, r')$, the solution for the electric field operator of a point source, and the bosonic creation and annihilation operators [3] as,

$$\begin{aligned} \hat{E}^+(r, \omega_P) &= i\omega_P^2\mu_0\sqrt{\frac{\hbar}{\pi}\epsilon_0}\int_{-\infty}^{\infty} dr'\sqrt{\epsilon_I(r', \omega_P)}\overleftrightarrow{G}(r, r') \cdot \hat{f}(r', \omega_P) \\ \hat{E}^-(r, \omega) &= -i\omega_P^2\mu_0\sqrt{\frac{\hbar}{\pi}\epsilon_0}\int_{-\infty}^{\infty} dr'\sqrt{\epsilon_I(r', \omega_P)}\overleftrightarrow{G}^*(r, r') \cdot \hat{f}^\dagger(r', \omega_P). \end{aligned} \quad (\text{S3})$$

Equations S1 and S3 allow us to write the time evolution of the bosonic annihilation operator using the Heisenberg Equation of motion as,

$$\begin{aligned} \dot{\hat{f}}(r, \omega_P) &= \frac{i}{\hbar} [\hat{H}, \hat{f}(r, \omega_P)] \\ &= -i\omega_P\hat{f}(r, \omega_P) + \omega_P^2\mu_0\sqrt{\frac{\hbar}{\pi}\epsilon_0}d(r_A)\sqrt{\epsilon_I(r, \omega_P)}\overleftrightarrow{G}^*(r_A, r, \omega_P)\hat{\sigma}_{ge}, \end{aligned} \quad (\text{S4})$$

where r_A is the position of the emitter in the waveguide. Formally integrating this equation from time t' to t results in [4],

$$\begin{aligned} \hat{f}(r, \omega_P, t) &= \hat{f}(r, \omega_P, t') \exp(-i\omega_P(t - t')) + \\ &\quad \omega_P^2\mu_0\sqrt{\frac{\hbar}{\pi}\epsilon_0}\int_0^t dt' d(r_A)\sqrt{\epsilon_I(r, \omega_P)}\overleftrightarrow{G}^*(r_A, r, \omega_P)\hat{\sigma}_{ge}(t')e^{-i\omega_P(t-t')}, \end{aligned} \quad (\text{S5})$$

where the first term describes a free excitation in the system that does not interact with the emitter, and the second term describes an interaction with the emitter either through a decay from excited to ground state or through a scattering event (virtual transition). Thus, we can write the electric field operator as,

$$\hat{E}^+ = \hat{E}_p^+ + \hat{E}_S^+, \quad (\text{S6})$$

where \hat{E}_p^+ represents the incident field and \hat{E}_S^+ represents the scattered field. The transmission coefficient for the light in the system is written in terms of the expectation values of these fields as,

$$t = \frac{\langle \hat{E}^+ \rangle}{\langle \hat{E}_p^+ \rangle}, \quad (\text{S7})$$

and the phase shift on the light from the interaction with the emitter is,

$$\phi = \arg(t). \quad (\text{S8})$$

Equations S3 and S5, with the help of the Green's tensor identity [3] and Kramer's Kronig relations [5], allow the scattered field in terms of the incident field as,

$$\hat{E}_S^+(r, t) = \frac{1}{\hat{\Omega}_P} g(r, r_A, \omega_A) \hat{\sigma}_{ge}(t) \hat{E}_p^+(r_A, t), \quad (\text{S9})$$

where we have defined the Rabi frequency operator as $\hat{\Omega}_P = d^* \cdot \hat{E}_p^+ / \hbar$, where $\langle \hat{\Omega}_P \rangle = \Omega_P$, and we use the dipole-projected Green's function [3],

$$g(r_i, r_j, \omega) = \frac{\mu_0 \omega^2}{\hbar} d^*(r_i) \cdot G(r_i, r_j, \omega) \cdot d(r_j). \quad (\text{S10})$$

For a chirally coupled quantum dot, the dipole projected Green's function becomes,

$$g(r, r_A, \omega) = i\Gamma(\Theta(r_A - r)\beta_L + \Theta(r - r_A)\beta_R) e^{ik_p|r-r_A|}, \quad (\text{S11})$$

where Θ is the Heaviside function and we define the couplings for photons moving left β_L and for photons moving right β_R as,

$$\beta_L = \frac{\Gamma_L}{\Gamma} = \frac{\Gamma_L}{\Gamma_L + \Gamma_R + \Gamma_{Loss}}, \quad (\text{S12})$$

$$\beta_R = \frac{\Gamma_R}{\Gamma} = \frac{\Gamma_R}{\Gamma_L + \Gamma_R + \Gamma_{Loss}}. \quad (\text{S13})$$

In the low-power regime (weak coherent beam) where $\Omega_P \rightarrow 0$, the scattering event that imparts a phase shift will dominate over spontaneous emission, allowing the emitter to act as a phase shifter. From Equations S2 and S7 the transmission coefficient becomes,

$$t = 1 - \Gamma\beta_R \frac{\Gamma_2 + i\Delta_P}{\Gamma_2^2 + \Delta_P^2}, \quad (\text{S14})$$

where we have defined the forward direction as right for simplicity. The phase shift can then be calculated with Equation S8. With the same assumptions, the observable transmission, T , can be written as,

$$T = \frac{\langle \hat{E}^- \hat{E}^+ \rangle}{\langle \hat{E}_p^- \hat{E}_p^+ \rangle} \quad (\text{S15})$$

$$T = 1 - 2\Gamma\Gamma_2 \frac{\beta_R(1 - \beta_R)}{(\Gamma_2^2 + \Delta_P^2)}.$$

2. IDEAL PHASE SOLUTION USING UNITARY DECOMPOSITION

To solve the ideal phase shifts for a target unitary we follow the decomposition and recombination method proposed by Clements et al. [6] where an ideal MZI is built up from the 2×2 transfer matrices of two 50 : 50 directional couplers and two phase shifters ($\phi, 2\theta$) as,

$$\begin{aligned} \text{MZI} &= \frac{1}{\sqrt{2}} \begin{bmatrix} 1 & i \\ i & 1 \end{bmatrix} \begin{bmatrix} e^{i2\theta} & 0 \\ 0 & 1 \end{bmatrix} \frac{1}{\sqrt{2}} \begin{bmatrix} 1 & i \\ i & 1 \end{bmatrix} \begin{bmatrix} e^{i\phi} & 0 \\ 0 & 1 \end{bmatrix} \\ &= ie^{i\theta} \begin{bmatrix} e^{i\phi} \sin\theta & \cos\theta \\ e^{i\phi} \cos\theta & -\sin\theta \end{bmatrix}, \end{aligned} \quad (\text{S16})$$

which can be expanded into the $N \times N$ matrix,

$$T_{m,n}^{(p)} = \begin{bmatrix} 1 & 0 & \dots & \dots & \dots & 0 \\ 0 & \ddots & \dots & \dots & \dots & \vdots \\ \vdots & \dots & ie^{i\theta} e^{i\phi} \sin\theta & ie^{i\theta} \cos\theta & \dots & \vdots \\ \vdots & \dots & ie^{i\theta} e^{i\phi} \cos\theta & -ie^{i\theta} \sin\theta & \dots & \vdots \\ \vdots & \dots & \dots & \dots & \ddots & 0 \\ 0 & \dots & \dots & \dots & 0 & 1 \end{bmatrix}, \quad (\text{S17})$$

representing the p th MZI between modes m and n in the circuit. To solve for the ideal phases the Clements method [6] then decomposes the unitary into a diagonal matrix D by applying MZIs/inverse MZIs using each of the $N(N-1)/2$ MZIs to nullify an off-diagonal entry. The result for a 4×4 unitary is,

$$\tilde{T}_{3,4}^{(1)} \tilde{T}_{2,3}^{(1)} U T_{1,2}^{(0)-1} T_{3,4}^{(0)-1} T_{2,3}^{(0)-1} T_{1,2}^{(1)-1} = D, \quad (\text{S18})$$

where the $\tilde{}$ indicates that these MZIs do not correspond to the hardware MZIs as they will be changed during the recombination steps. To determine the required phases for these MZIs, the algorithm is as follows; If a $T_{m,n}^{(p)-1}$ is being applied, the phases are chosen as,

$$\begin{aligned} \theta &= \frac{\pi}{2} - \arctan \left(\left| \frac{U_{Null}[x,m]}{U_{Null}[x,n]} \right| \right) \\ \phi &= \pi + \arg \left(\frac{U_{Null}[x,m]}{U_{Null}[x,n]} \right), \end{aligned} \quad (\text{S19})$$

where U_{Null} corresponds to the partially decomposed matrix at the current decomposition step, and the index x is the row index of the element being nullified. Conversely, if a $T_{m,n}^{(p)}$ is being applied to the LHS, the phases are chosen as,

$$\begin{aligned} \theta &= \frac{\pi}{2} - \arctan \left(\left| \frac{U_{Null}[n,y]}{U_{Null}[m,y]} \right| \right) \\ \phi &= \pi + \arg \left(\frac{U_{Null}[n,y]}{U_{Null}[m,y]} \right), \end{aligned} \quad (\text{S20})$$

where now the column index y corresponds to the column of the element being nullified.

For the recombination step, isolate for U in Equation S18, and shift the diagonal matrix to the left, replacing it and the $\tilde{T}_{m,n}^{(p)-1}$'s according to,

$$\tilde{T}_{m,n}^{(p)-1} D = D_1 T_{m,n}^{(p)}, \quad (\text{S21})$$

where D_1 is another diagonal matrix and $T_{m,n}^{(p)}$ is the MZI that corresponds to the hardware implementation. The new phases for $T_{m,n}^{(p)}$, following the Clements solution are,

$$\begin{aligned} \theta &= \frac{\pi}{2} - \arctan \left(\left| \frac{M[n,m]}{M[n,n]} \right| \right) \\ \phi &= \pi + \angle \frac{M[n,m]}{M[n,n]}, \end{aligned} \quad (\text{S22})$$

where $M = \tilde{T}_{m,n,p}^{-1}D$. From here, we determine the new diagonal matrix as,

$$D_1 = \tilde{T}_{m,n}^{(p)-1}DT_{m,n}^{(p)-1}. \quad (\text{S23})$$

By repeating these steps until D is on the left side of the formula, we get, for a 4×4 , an equation for the ideal unitary as,

$$U = D'T_{2,3}^{(1)}T_{3,4}^{(1)}T_{1,2}^{(1)}T_{2,3}^{(0)}T_{3,4}^{(0)}T_{1,2}^{(0)}, \quad (\text{S24})$$

where we have relabelled the final diagonal matrix as D' , which corresponds to global phase shifts applied at the end of the MZI mesh.

3. IMPERFECT TRANSFER MATRIX GENERATION

Imperfections are added to the transfer matrices at the MZI level, which combine to form an imperfect transfer matrix using Equation S24. The first imperfection we consider is nanophotonic loss, originating from waveguide propagation losses and beam splitter losses. For this, we use the common [7–10] assumption that loss is balanced across MZI paths, modeling the loss as,

$$Loss = \begin{bmatrix} \sqrt{1-L} & 0 \\ 0 & \sqrt{1-L} \end{bmatrix}. \quad (\text{S25})$$

Beam splitter error on the directional couplers is also included, modeled using the standard variable beam splitter matrix,

$$BS = \begin{bmatrix} \sqrt{r} & i\sqrt{1-r} \\ i\sqrt{1-r} & \sqrt{r} \end{bmatrix}, \quad (\text{S26})$$

where r is the reflectivity of the beam splitter and $r = 0.5$ in the ideal case.

Quantum dot phase shift imperfections are factored into the model as well. Imperfect coupling, $\beta = \beta_L + \beta_R < 1$, and imperfect directionality, $D = (\beta_R - \beta_L)/(\beta_L + \beta_R) < 1$, are included through their effects on quantum dot loss, modeled as $\gamma = 1 - T$, where T is the observable transmission in the system calculated using Equation S15. This is included using the lossy phase shift matrix,

$$PS = \begin{bmatrix} \sqrt{1-\gamma}e^{i\phi} & 0 \\ 0 & 1 \end{bmatrix}. \quad (\text{S27})$$

Figure S1 depicts how the quantum dot loss γ is sampled for each phase shifter from a distribution with a central value $\gamma = 1 - T$ with a standard deviation of 5% of the central value to model fluctuations between different quantum dots. Combining all these imperfections into the model, each MZI is calculated using the imperfect matrix,

$$MZI = \begin{bmatrix} \sqrt{r_2} & i\sqrt{1-r_2} \\ i\sqrt{1-r_2} & \sqrt{r_2} \end{bmatrix} \begin{bmatrix} \sqrt{1-\gamma_2}e^{i2\theta} & 0 \\ 0 & 1 \end{bmatrix} \begin{bmatrix} \sqrt{r_1} & i\sqrt{1-r_1} \\ i\sqrt{1-r_1} & \sqrt{r_1} \end{bmatrix} \begin{bmatrix} \sqrt{1-\gamma_1}e^{i\phi} & 0 \\ 0 & 1 \end{bmatrix} \begin{bmatrix} \sqrt{1-L} & 0 \\ 0 & \sqrt{1-L} \end{bmatrix}, \quad (\text{S28})$$

which is then combined with all other imperfect MZIs to build an $N \times N$ imperfect transfer matrix. This is depicted as a circuit in Figure S1a, which shows how MZIs combine to form a 4×4 circuit, where Figure S1c shows the breakdown of each MZI component with its appropriate transfer matrix.

This imperfect transfer matrix does not include dephasing and spectral diffusion, which are included in QD imperfections. Dephasing provides a chance of having an incoherent interaction with an average phase shift of 0, calculated as $|\alpha_{\text{inc}}|^2 = (T - |t|^2)/T$. Consequently, the probability of a coherent interaction is $|\alpha_{\text{co}}|^2 = 1 - |\alpha_{\text{inc}}|^2$. Figure S2 depicts the coherence probability based on dephasing and directionality for detunings of $\Delta_p = 0\Gamma$ in Figure S2a and $\Delta_p = 0.3\Gamma$ in Figure

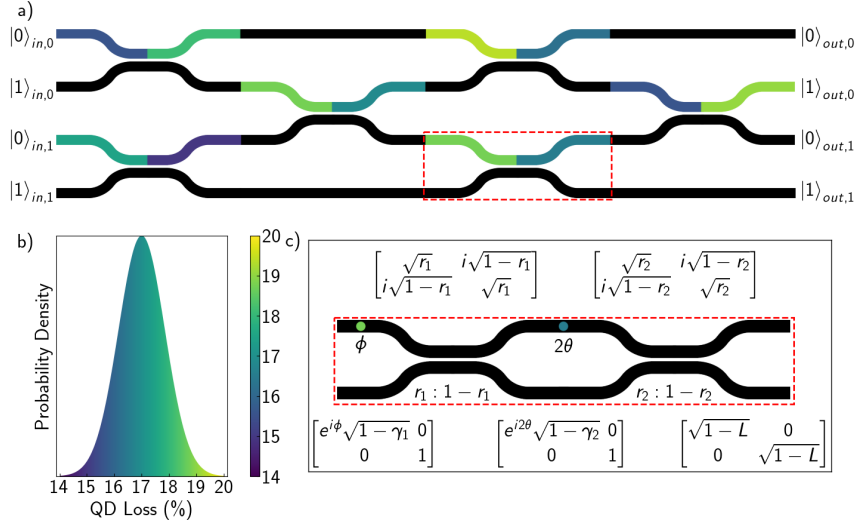


Fig. S1. Imperfect circuit transfer matrix generation with example quantum dot loss distribution. (a) 4×4 MZI mesh circuit depicting QD loss for each quantum dot in the MZIs. The color in the top-left branch of each MZI indicates the loss for the ϕ phase shifter, and the color in the top-right branch of each MZI indicates the loss for the 2θ phase shifter. If the path is black this indicates no QD loss in that region of the circuit. (b) Normal distribution for QD loss with a central value of 17% and a standard deviation of 5% of 17%. (c) MZI with transfer matrices for the two QD phase shifters with losses γ_1 and γ_2 as colored, the two beam splitters with reflectivities r_1 and r_2 and nanophotonic loss per MZI of L .

S2. The larger the detuning, the higher the coherence probability, since there is less interaction with the quantum dot and thus less dependence on dephasing.

Dephasing is modeled using a Monte-Carlo simulation with 500 samples, where in each trial each phase shifter is sampled to be on/off based on its QD's incoherence probability, generating 500 imperfect unitaries on which we average the performance.

Spectral diffusion is also included in these Monte-Carlo simulations, where for each phase shifter we sample a shift in detuning, and consequently phase, from a normal distribution with a standard deviation of σ_{SD} , modeling the fluctuations from spectral diffusion in the system. Figure S3 depicts the spectral diffusion effects on detuning and phase shift for an example spectral diffusion of $\sigma_{SD} = 0.06\Gamma$. The detuning shift is sampled from the normal distribution shown in Figure S3a, with Figure S3b showing the phase shift distribution for phase shifts of π and $\pi/2$, and Figure S3c showing a sample MZI pre and post spectral diffusion shift. It is evident that large phase shifts (like π) where $\Delta_p \rightarrow 0$ will have large fluctuations since detuning will often change signs, whereas smaller phase shifts with larger detuning such as $\pi/2$ will not see as much spectral diffusion influence.

4. CIRCUIT ACCURACY MEASUREMENT METHODS AND PHASE OPTIMIZATION

The accuracy of an imperfect transfer matrix (non-ideal U) for each circuit is calculated using the matrix infidelity [6],

$$\mathcal{I} = 1 - \left| \frac{\text{tr}(U^\dagger U_{\text{non}})}{\sqrt{N \text{tr}(U_{\text{non}}^\dagger U_{\text{non}})}} \right|^2, \quad (\text{S29})$$

which excludes balanced losses, allowing us to focus on accuracy over count rate. However, for the CZ and CNOT gate, we consider accuracy using the post-selected output state infidelity instead. Since the CNOT and CZ are two-photon gates, their matrices must be converted into the fock basis by calculating the matrix permanent [11]. However, only four inputs/outputs of these expanded matrices correspond to the computational two-qubit basis states $\{|00\rangle, |01\rangle, |10\rangle, |11\rangle\}$.

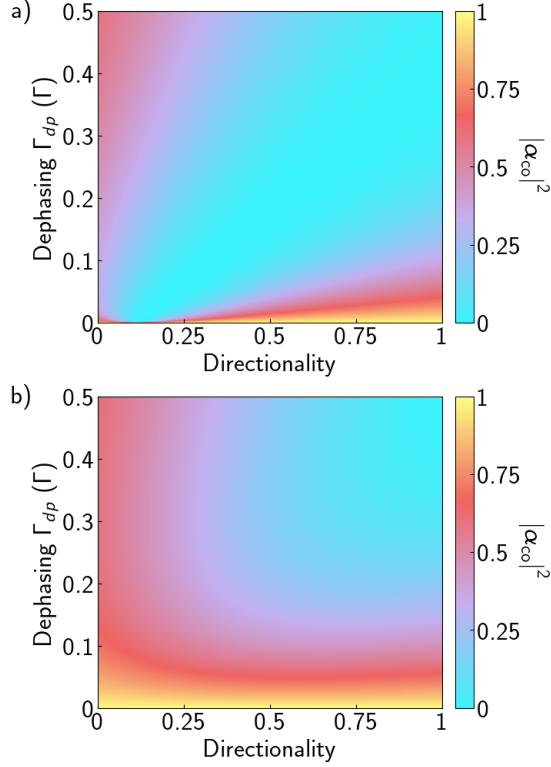


Fig. S2. Coherent phase shift probability ($|\alpha_{\text{co}}|^2$) maps spanning dephasing (0Γ to 0.5Γ) and directionality (0 to 1) with coupling of $\beta = 0.9$ (a) $\Delta_P = 0\Gamma$ (b) $\Delta_P = 0.3\Gamma$.

Thus, for each input-output pair, we calculate the unconditional output state following the equation,

$$|\psi_{\text{out,non}}^{(i,\text{unc})}\rangle = U_{\text{non}}|\psi_{\text{in}}^{(i)}\rangle, \quad (\text{S30})$$

where $|\psi_{\text{out,non}}^{(i,\text{unc})}\rangle$ is the imperfect unconditional output state in the fock basis, and $U_{\text{non}}, \psi_{\text{in}}^{(i)}$ are also in the fock basis. These states are then post-selected by truncating them down to the computational basis states resulting in four-entry vectors and re-normalizing them. The conditional output state infidelity for an input-output pair is then calculated using,

$$\mathcal{I}_i^{(\text{con})} = 1 - \left| \langle \psi_{\text{out}}^{(i,\text{con})} | \psi_{\text{out,non}}^{(i,\text{con})} \rangle \right|^2. \quad (\text{S31})$$

We also consider the post-selected 4×4 computational basis matrices in the main text, which are found by truncating the fock basis matrix down to the 4×4 matrix corresponding to the four computational basis inputs and outputs and re-normalizing the matrix.

To perform phase shift optimization on these circuits, we use the appropriate cost function (Equation S29 or S31) to measure the circuit error, and perform an optimization on all phases using the BOBYQA optimization algorithm [12]. To do this, we began by determining the phase shifts for a given unitary in the ideal case using the Clements decomposition method outlined in Section 2. Then, imperfections were added to the circuit to calculate the imperfect transfer matrix and its associated infidelity. For optimization, the ideal phases were chosen as initial phase guesses, with phase constraints of $[-\pi, \pi]$, which are required as this is a constrained optimization algorithm. When optimizing circuits with dephasing/spectral diffusion, the cost function averages the infidelity for 500 sampled matrices to find the cost for every optimization step.

5. CNOT GATE RESULTS

Similar to the results for the CZ gate in the main text, here we consider the unheralded CNOT gate, a 6-mode circuit with $1/9$ probability of success. The performance was first measured using the

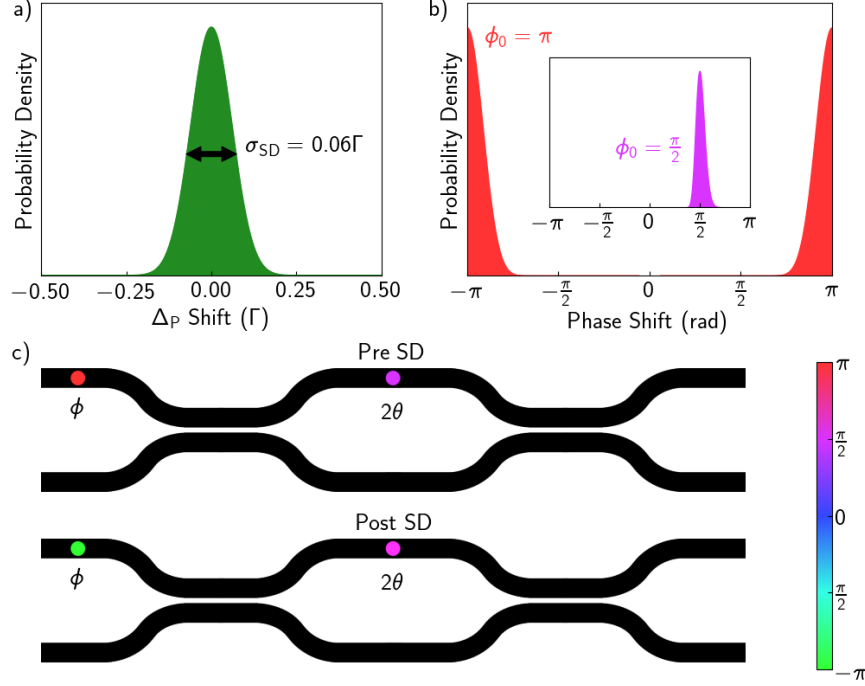


Fig. S3. Spectral Diffusion effects on detuning and phase shift for $\sigma_{SD} = 0.06\Gamma$. (a) Normal distribution for detuning shift from spectral diffusion. (b) Phase shift distribution example for initial phases of π and $\pi/2$ (inset). (c) Example MZI with initial phases of $\phi = \pi$ and $2\theta = \pi/2$ before and after sampling spectral diffusion.

matrix infidelity (Equation S29) spanning from dephasing of $\Gamma_{dp} = 10^{-8}\Gamma \rightarrow 10^{-1}\Gamma$ for nanophotonic, state-of-the-art and typical imperfections as shown in Figure S4. These imperfections are the same as listed in the main text. The results show that performance and optimization depend heavily on dephasing, where incoherent interactions heavily hinder performance. However, state-of-the-art quantum dot imperfections can be optimized to perform on par with nanophotonic imperfections with no dephasing. Next, as described in Section 4, the CNOT gate circuit was optimized based on the average conditional output state infidelity (Equation S31). The optimized post-selected 4×4 computational basis matrices for nanophotonic, state-of-the-art, and typical imperfections are shown in Figure S4b-d, along with their optimized conditional output state infidelities. The output state performance is near perfect for nanophotonic and state-of-the-art imperfections, despite overall performing poorer than the CZ due to increased circuit complexity.

6. RANDOM CIRCUIT INFIDELITY DISTRIBUTIONS

Each infidelity data point in the results is the result of a beta distribution across 100 Haar random unitary matrices to simulate random circuit performance accurately. A beta distribution is used to accurately average the data as the infidelity distribution across 100 samples is asymmetric and includes outliers. A beta distribution follows the probability density function,

$$f(x) = \frac{(x-a)^{p-1}(b-x)^{q-1}}{B(p,q)(b-a)^{p+q-1}}, \quad (\text{S32})$$

where a and b are the lower and upper bounds on x , p and q are shape parameters where $p, q > 0$ and $B(p, q)$ is the beta function that follows the equation,

$$B(\alpha, \beta) = \int_0^1 t^{\alpha-1}(1-t)^{\beta-1} dt. \quad (\text{S33})$$

Figure S5 shows an example infidelity histogram for an $N = 4$ circuit with an arbitrary choice of 2.3% beam splitter error. This figure also plots a beta fit, normal distribution fit, and the mean of

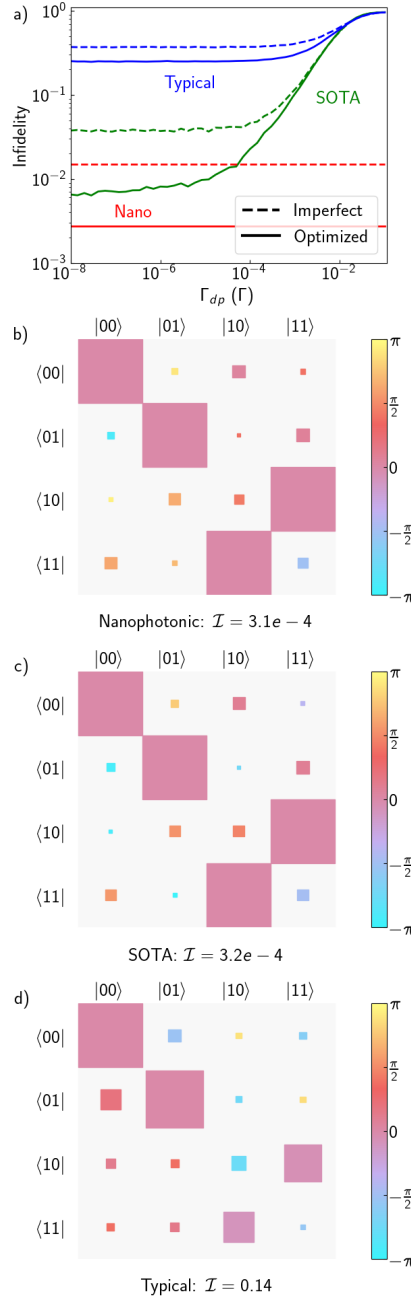


Fig. S4. Unheralded CNOT performance for nanophotonic, state-of-the-art, and typical imperfections. (a) Matrix infidelity as a function of dephasing. The nanophotonic infidelities with no dephasing are shown as horizontal lines across the figure. (b-d) Optimized nanophotonic, state-of-the-art, and typical post-selected 4×4 computational basis matrices for the unheralded CNOT gate, with conditional output state fidelities listed.

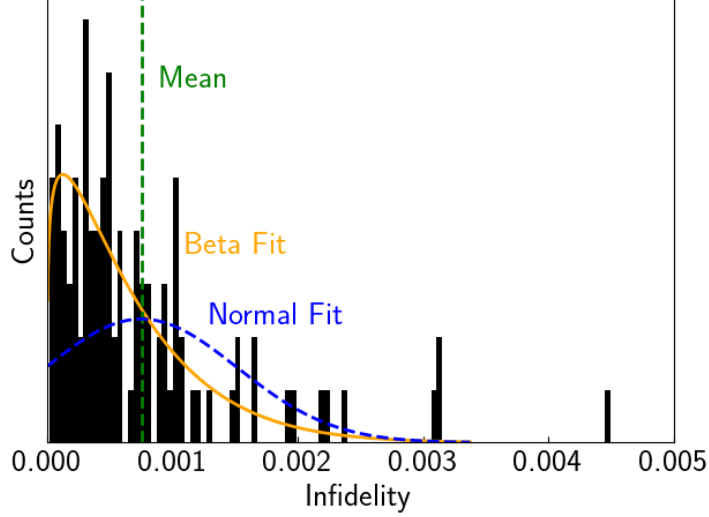


Fig. S5. Matrix infidelity histogram over 100 Haar random $N = 4$ circuits for a beam splitter error of 2.3%, with no other imperfections. Here we show the mean of the data (green), a beta fit (orange), and a normal fit (blue), to the data.

the data. The mean and normal fit in Figure S5 both result in average infidelity that is higher than the majority of the data. Conversely, the beta fit accounts for the asymmetry, representing the data accurately. Thus, the mean of the beta fit is used for random circuit infidelity results.

7. LINEAR RESPONSE PULSE WIDTH CONSTRAINT

The scattering of few-photon Fock states by a two-level system chirally-coupled to a one-dimensional waveguide can be described using an input-output formalism, as demonstrated in [13]. Here, we will use the scattering matrices for one and two-photon Fock states to demonstrate the linear phase response that arises when the photon pulse width σ_p is much less than the linewidth of the quantum emitter Γ . Then, we select a practical constraint for σ_p where the emitter can be used as a linear phase shifter for Fock states of up to two photons. For simplicity, we will assume perfect directionality and no loss.

As shown in [13], the single-photon scattering matrix elements are given by,

$$\langle p | S | q \rangle = t(q) \delta(q - p) \quad : \quad t(q) \equiv \frac{q - \omega_A - \frac{i\Gamma}{2}}{q - \omega_A + \frac{i\Gamma}{2}}, \quad (\text{S34})$$

where S is the scattering matrix, $|q\rangle = a_q^\dagger |0\rangle$, and ω_A is the transition frequency of the quantum emitter. Consider a single-photon wave packet with a pulse shape $\alpha(\omega)$, centered at angular frequency ω_0 , as the input state,

$$|\text{in}\rangle_1 = \int_{-\infty}^{\infty} d\omega \alpha(\omega) a_\omega^\dagger |0\rangle. \quad (\text{S35})$$

The output state can be derived as,

$$|\text{out}\rangle_1 = \int_{-\infty}^{\infty} d\omega t(\omega) \alpha(\omega) a_\omega^\dagger |0\rangle, \quad (\text{S36})$$

by first applying the scattering matrix to the input, then inserting closure followed by Eq. S34. Most commonly, $\alpha(\omega)$ will take either a Gaussian or Lorentzian form, both of which can be parameterized by width σ_p . For either form, $\alpha(\omega) \sim \delta(\omega - \omega_0)$ in the limit $\sigma_p \rightarrow 0$ which implies,

$$|\text{out}\rangle_1 \sim t(\omega_0) a_{\omega_0}^\dagger |0\rangle. \quad (\text{S37})$$

In the lossless case, $|t(\omega)| = 1$ and $\arg\{t(\omega)\}$ varies with detuning $\Delta = \omega_A - \omega_0$ from $-\pi$ to π . Therefore, the quantum emitter acts as a perfect phase shifter when acting on single-photon Fock states in the monochromatic limit.

We now turn to the two-photon scattering matrix elements, derived in Ref. [13] as,

$$\begin{aligned} \langle p_1 p_2 | S | q_1 q_2 \rangle = & t(p_1) t(p_2) [\delta(q_1 - p_1) \delta(q_2 - p_2) + \delta(q_1 - p_2) \delta(q_2 - p_1)] \\ & + \frac{i\sqrt{\Gamma}}{\pi} s(p_1) s(p_2) [s(q_1) + s(q_2)] \delta(q_1 + q_2 - p_1 - p_2), \end{aligned} \quad (\text{S38})$$

where $|q_1 q_2\rangle = \frac{1}{\sqrt{2}} a_{q_1}^\dagger a_{q_2}^\dagger |0\rangle$ and $s(\omega)$ is a measure of the excitation of the emitter by a single-photon wave packet, defined by,

$$s(\omega) \equiv \frac{\sqrt{\Gamma}}{q - \omega_A + \frac{i\Gamma}{2}}. \quad (\text{S39})$$

With the input as the two-photon analog of Eq. S35,

$$|\text{in}\rangle_2 = \frac{1}{\sqrt{2}} \int_{-\infty}^{\infty} d\omega_1 \int_{-\infty}^{\infty} d\omega_2 \alpha(\omega_1) \alpha(\omega_2) a_{\omega_1}^\dagger a_{\omega_2}^\dagger |0\rangle, \quad (\text{S40})$$

the output can be derived by following the same procedure to obtain the result,

$$\begin{aligned} |\text{out}\rangle_2 = & \frac{1}{\sqrt{2}} \int_{-\infty}^{\infty} d\omega_1 \int_{-\infty}^{\infty} d\omega_2 \left[t(\omega_1) t(\omega_2) \alpha(\omega_1) \alpha(\omega_2) + \frac{i\sqrt{\Gamma}}{2\pi} s(\omega_1) s(\omega_2) \right. \\ & \left. \times \int_{-\infty}^{\infty} dp \alpha(\omega_1 + \omega_2 - p) \alpha(p) (s(\omega_1 + \omega_2 - p) + s(p)) \right] a_{\omega_1}^\dagger a_{\omega_2}^\dagger |0\rangle. \end{aligned} \quad (\text{S41})$$

This output state consists of the sum of a purely uncorrelated part with a part that features correlations between the photons, however, these parts are not orthogonal. Therefore, it is not trivial to show analytically that only a linear phase response occurs in the limit $\sigma_p \rightarrow 0$. Instead, given that the input state is purely uncorrelated, we plot the input-output overlaps in Fig. S6 for

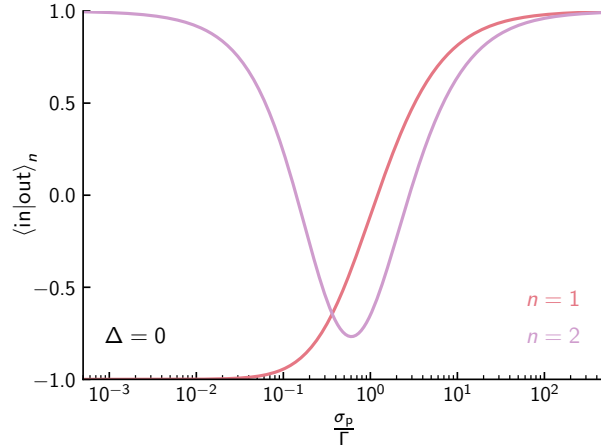


Fig. S6. Overlap between an input uncorrelated n -photon wave packet with Lorentzian pulse shape and the output state achieved after the photons scatter from a perfectly chiral two-level quantum emitter coupled to a 1D waveguide, as a function of pulse width σ_p . Each photon is assumed to be centered on resonance with the quantum emitter transition frequency such that $\Delta = \omega_A - \omega_0 = 0$, and the interaction is assumed to be lossless.

one and two-photon Fock states as a function of σ_p assuming a Lorentzian pulse shape,

$$\alpha(\omega) = \sqrt{\frac{2}{\pi}} \frac{\sqrt{\sigma_p^3}}{\sigma_p^2 + (\omega - \omega_0)^2}, \quad (\text{S42})$$

for convenience, yet without loss of generality in the limit $\sigma_p \rightarrow 0$, and resonance such that $\omega_A = \omega_0$. We find that these overlaps are purely real for all σ_p , and are able to clearly identify the desired linear phase response,

$$|\text{out}\rangle_n = e^{i \arg\{t(\omega_0)\}} |\text{in}\rangle_n, \quad (\text{S43})$$

for $\sigma_p \leq 0.001\Gamma$, where $\arg\{t(\omega_0)\} = \pi$ on resonance. Specifically, the magnitudes of the input-output overlaps are both > 0.99 if this constraint is met.

REFERENCES

1. C. Gerry and P. L. Knight, *Introductory quantum optics* (Cambridge university press, 2005).
2. P. Meystre and M. Sargent, *Elements of quantum optics* (Springer Berlin Heidelberg, 2007).
3. A. Asenjo-Garcia, J. Hood, D. Chang, and H. Kimble, "Atom-light interactions in quasi-one-dimensional nanostructures: A green's-function perspective," *Phys. Rev. A* **95**, 033818 (2017).
4. H. T. Dung, L. Knöll, and D.-G. Welsch, "Resonant dipole-dipole interaction in the presence of dispersing and absorbing surroundings," *Phys. Rev. A* **66**, 063810 (2002).
5. D. Dzotjan, J. Kästel, and M. Fleischhauer, "Dipole-dipole shift of quantum emitters coupled to surface plasmons of a nanowire," *Phys. Rev. B* **84**, 075419 (2011).
6. W. R. Clements, P. C. Humphreys, B. J. Metcalf, W. S. Kolthammer, and I. A. Walmsley, "Optimal design for universal multiport interferometers," *Optica* **3**, 1460–1465 (2016).
7. W. Bogaerts, D. Pérez, J. Capmany, D. A. B. Miller, J. Poon, D. Englund, F. Morichetti, and A. Melloni, "Programmable photonic circuits," *Nature* **586**, 207–216 (2020).
8. J. Ewaniuk, J. Carolan, B. J. Shastri, and N. Rotenberg, "Imperfect Quantum Photonic Neural Networks," *Adv. Quantum Technol.* **6**, 2200125 (2023).
9. F. Shokraneh, S. Geoffroy-gagnon, and O. Liboiron-Ladouceur, "The diamond mesh, a phase-error- and loss-tolerant field-programmable mzi-based optical processor for optical neural networks," *Opt. Express* **28**, 23495–23508 (2020).
10. F. Shokraneh, M. Sanadgol Nezami, and O. Liboiron-Ladouceur, "Theoretical and Experimental Analysis of a 44 Reconfigurable MZI-Based Linear Optical Processor," *J. Light. Technol.* pp. 1–1 (2021).
11. S. Aaronson and A. Arkhipov, "The computational complexity of linear optics," (2010).
12. M. J. Powell *et al.*, "The BOBYQA algorithm for bound constrained optimization without derivatives," *Camb. NA Rep. NA2009/06*, Univ. Cambridge, Camb. **26** (2009).
13. S. Fan, Ş. E. Kocabaş, and J.-T. Shen, "Input-output formalism for few-photon transport in one-dimensional nanophotonic waveguides coupled to a qubit," *Phys. Rev. A* **82**, 063821 (2010).